

Mitigation of Dynamic Stall Using Small Controllable Devices

Tin-Chee Wong

Aerospace Engineer

US Army Research Development and Engineering Command

Aviation Engineering Directorate

Redstone Arsenal, AL 35898

tinchee.wong@us.army.mil

Abstract

The unsteady, compressible Reynolds-averaged Navier-Stokes equations, based on an unstructured-grid approach with one-equation Spalart-Allmaras, and two-equation Menter shear-stress-transport turbulence models, have been used to investigate flow over oscillating airfoils. The dynamic stall characteristics of the Boeing VR-7 airfoil without controllable devices were computed and compared with experimental data. Two actively controllable devices in the form of trailing-edge flap and leading-edge slat were analyzed for the same airfoil to mitigate dynamic stall effects. The addition of a trailing-edge flap on a VR-7 airfoil with sinusoidal motion about flap hinge opposite to the main oscillating airfoil can delay stall and reduce negative peak pitching moment. The addition of a stationary or moving leading-edge slat on a VR-7 airfoil completely eliminates the development of a dynamic vortex and enhances lift.

Introduction

The dynamic stall phenomenon has been known to be a major factor that limits helicopter rotor performance at high forward speed flight, in high gravitational force (“g”) maneuvers, and at high density-altitude because of the onset of large airloads and vibrations on the blades. Stall occurs on a helicopter rotor at relatively high airspeeds as the advancing and retreating blades begin to operate close to the attached flow limits. These limits are a direct result of the blade flapping and large pitching moments that characterize the performance of an airfoil operating through dynamic stall. Recent desert and mountainous region operations have challenged current helicopters with the requirement to operate effectively in high density-altitude conditions. Relieving the

limitation due to dynamic pitching moment stall through the use of an advanced airfoil such as VR-12, a control nose-droop concept¹ or a passive control device by means of a miniature button shape leading edge vortex generator² may provide useful increased rotor limits. Recent work done by the author³ was to seek low-cost method to alleviate dynamic stall using an adjoint optimization technique^{4, 5} to change upper surface of the airfoil to have better static characteristics and enable alleviation of the dynamic pitching moment divergence. The resulting modification provided significant pitch link load reduction based on C81 calculation. Another effort involved the application of a miniature trailing-edge device (in the form of a Gurney flap) to the lower surface of a VR-12 airfoil. Numerical results demonstrated the ability to alleviate dynamic stall⁶. Most single-element advanced airfoils are finely tuned shapes that produce high lift while maintaining acceptable pitching moments and drag

Presented at the American Helicopter Society
Aeromechanics Specialists’ Conference, San
Francisco, CA, January 20-22, 2010.

This is a work of the U. S. Government and is not
subject to copyright protection.

levels. In order to address the need to develop main rotors that will allow greater payload capability, higher forward flight speeds, increased range and endurance, and greater maneuverability and agility, multi-element airfoils must be considered. It was known from literature and fixed-wing applications that lift of an airfoil at high angles of attack can be enhanced by segmenting an airfoil into multiple elements. Recent published work⁷ showed that the slat relieves the adverse pressure gradient on the nose of the main element to delay separation, and also eliminate completely the development of a dynamic-stall vortex during unsteady motions. The objective of the current work is to explore two actively controllable devices in the form of a trailing-edge flap and a leading-edge slat on the VR-7 airfoil to mitigate dynamic stall effects. A strategy for the leading edge slat schedule and flap actuation during pitching oscillation has been developed to obtain better dynamic stall characteristics for rotor blade application.

Solution Algorithm

The unstructured mesh flow solver used in this study is FUN3D. This flow solver has been developed and supported by the NASA Langley Research Center. The governing equations are the three-dimensional, unsteady, compressible Reynolds-averaged Navier-Stokes equations. The Spalart and Allmaras (S-A), and the Menter Shear-Stress-Transport^{8, 9} $k-\omega$ (SST) turbulence models are used for the second closure. The detail of the discretization approach used in FUN3D is in references 10 and 11. The code uses an implicit, upwind, finite-volume discretization in which the dependent variables are stored as mesh vertices. Inviscid fluxes at cell interfaces are computed using the flux-differencing scheme of Roe¹² and viscous fluxes are evaluated by using an approach equivalent

to a central-difference Galerkin procedure. For steady-state flows, temporal discretization is performed by using a backward Euler time-stepping scheme. At each time step, the linear system of equations is approximately solved with an implicit line relaxation scheme¹¹. A local time-step technique is employed to accelerate convergence to a steady-state solution. For the time-accurate pitching oscillation, a generalized backward difference scheme is used to construct a higher order temporal scheme by extending the difference stencil in time¹³. A temporal error control method is implemented as an exit criterion for the sub-iterative loop of the dual time stepping process. For all unsteady pitching cases presented in this paper, the solution is second order accurate in time and space and the specified fraction of temporal error control is 0.15.

The airfoil pitching motion was simulated by oscillating the entire grid about the quarter-chord location with the given pitching rate. For an airfoil with a leading-edge slat and a trailing-edge flap, the motion was handled through deforming mesh relative to the main body within the mesh. The deforming mesh computation utilizes the geometric conservation law to ensure the scheme is free-stream preserving with moving meshes.

Each simulation was performed by first computing the steady-state solution at the mean angle of attack. This solution then became initial condition for an unsteady simulation that was performed using a second-order, dual-time-stepping procedure. The periodic solution was obtained at the fourth cycle with 2000 steps per cycle.

Results

All meshes used in this study were generated using the AFLR grid generator

developed by Mississippi State University¹⁴. The meshing strategies, requirements of grid-density and time-step for unsteady calculation remain the same as reported in Reference 3. The airfoil sections used for this study were VR-7, VR-7 with leading-edge slat,^{7, 15} and VR-7 with trailing-edge flap airfoil sections. The unstructured meshes of VR-7 airfoil are shown in Figure 1. The baseline airfoil without slat and flap is shown in Figure 1a. Airfoils with leading-edge slat and trailing-edge flap are shown in Figure 1b and 1c, respectively. The initial off-surface spacing of all meshes is 10^{-6} chord length and the extent of the outer domain is 20 chords from the center of the airfoil.

Unsteady Validation Case

An unsteady pitching case was chosen to represent the tunnel test case¹⁶ of frame 49120 (F49120) for VR-7 baseline airfoil section. The purpose was to investigate the effect of turbulence models on the lift, drag and pitching moment coefficients. The airfoil is pitched sinusoidally about the quarter chord, according to

$$\alpha = \alpha_m + \alpha_o \sin(2kM_\infty t)$$

where α is the instantaneous angle of attack, α_m is the mean angle of attack, α_o is the pitch amplitude and k is the reduced frequency. The reduced frequency is normalized by the half-chord length. This dynamic stall case of free-stream Mach number of 0.185 is defined by the parameter set $\alpha_m = 15^\circ$, $\alpha_o = 10^\circ$ and $k = 0.1$. Figure 2 shows the hysteresis of lift (left), drag (right) and pitching moment (bottom) of the VR-7 airfoil using S-A, and SST turbulence models. Both solutions show a large nose-down moment (Figure 2c) at $\alpha = 23^\circ$ and a corresponding drag rise (Figure 2b), which indicates the formation of a stall vortex from the trailing edge and rapid convection to

downstream. The predicted results have a 3° delay in stall angle as compared with the experiment. All computed lift-curve slopes do not compare well with the tunnel data which may be attributed to the wind tunnel wall effects. The dynamic lift curve obtained from SST model shows a double peak in lift before the moment divergence occurs. This trend is also evident in the experimental data and there is a discrepancy of about 3° in pitch angle. The computed magnitude of peak values of lift, drag and moment from SST turbulence model shows relatively better correlation with the experimental data than the one-equation turbulence model of S-A.

Six pitch angles were chosen to compare surface-pressure coefficient (C_p) computations with tunnel test data. The corresponding lift and pitching moment at the selected α is shown in Figure 3. Figure 4 presents the comparison of surface-pressure coefficient from the SST and S-A turbulence models with the experimental data. A black symbol is used to denote experimental data, and lines indicate computed results. The plots in the left and right columns stand for pitch up and pitch down motion of the cycle, respectively. The computed SST and S-A results are fairly similar except at the maximum pitch angle of 25° . The angles of 23.73° and 24.68° are the corresponding double peak in the lift coefficient (Figure 3). The experimental data shows the upstream movement of adverse pressure gradient from the trailing edge at $\alpha = 23.73^\circ$ and the stall vortex moves aft over the upper surface of the airfoil at $\alpha = 24.68^\circ$. The spike of C_p at $\alpha = 24.68^\circ$ indicates that the stall vortex traveling over the trailing edge. Similar phenomenon occurs at the SST result at $\alpha = 24.89^\circ$ at beginning of pitch down cycle. The corresponding computed pressure contour plots of the selected pitch angles are shown in Figure 5. Pressure-

coefficient contour plots at angles of 23.76° and 24.69° indicate the formation of a stall vortex at the trailing edge. These angles are the close to the corresponding double peak in dynamic lift curve in Figure 3. The right-column of Figure 5 indicates the stall is followed by an extensive amount of separation that lingers throughout the down-stroke portion of the cycle until reattached flow is obtained at about $\alpha=5^\circ$. The instantaneous streamlines plots colored by Mach number also indicate the trailing-edge separation bubble moves toward the leading edge of the airfoil, and the vorticity accumulates until reaching a point when the stall vortex sheds downstream (Figure 6).

The main objective was to demonstrate the feasibility of small controllable devices to mitigate this dynamic stall phenomenon. Even though results using the SST turbulence model were not compared well with the experimental data; however, this turbulence model did demonstrate the ability to capture the physics of dynamic stall and then was chosen for dynamic stall mitigation study.

VR-7 with Controlled Trailing-Edge Flap

The effects of trailing-edge flap configurations on lift, drag and pitching moments during unsteady pitching oscillation was investigated using VR-7 airfoil with a flap layout as shown in Figure 7. The flap overhang is X_f and the maximum amplitude of flap deflection angle is δ_f . The flap is rotated sinusoidally about flap hinge at frequency of k_f . The parameter of X_f and the flap size is set to 0.5% and 7.7% of chord length, respectively. A total of four cases were computed at the same flow condition using the SST turbulence model. Three cases were computed with δ_f of 0° , 5° and 10° at $k_f=0.1$ in opposite rotational direction of the main airfoil.

Figure 8 show the comparison of lift and pitching moment coefficients of VR-7 baseline and modified airfoils with trailing-edge flap in different actuations. The computed results of the baseline VR-7 airfoil with and without stationary flap (flap $\delta_f=0^\circ$) are plotted in red and green lines, respectively. There exists a clearance between the modified VR-7 airfoil and flap due to flap overhang. The dynamic lift shows the same lift-curve slope except for angles above 17° . There is a reduction in negative peak moment for stationary flap (flap $\delta_f=0^\circ$) as compared with the baseline VR-7. It indicates the small clearance has a release effect on the dynamic stall behavior. The moment- α loop shows that there is a decrease in peak negative pitching moment and delay stall as the flap deflecting upward during the up-stroke cycle. The largest decrease in moment occurs with the maximum δ_f of 10° .

Comparing the pressure coefficient contour plots of Figures 5 and 9, the case of $\delta_f=10^\circ$ has a weaker stall vortex than baseline airfoil and airfoil with the one of $\delta_f=0^\circ$. However, the increase in δ_f also has reverse effect on the dynamic lift advantage and pitching moment at the low angle of attack region. Another case was performed with flap actuation scheduled such that there is no flap motion beyond the tab angle of the baseline airfoil during the down-stroke cycle. The lift- α and pitching-moment- α curves for the cases with controlled flap actuation and the baseline airfoil with $\delta_f=0^\circ$ are shown in Figure 10. The controlled flap actuation (flap-control $\delta_f=10^\circ$) case has similar lift and pitching moment characteristics to the case of $\delta_f=0^\circ$ at low angle of attack region, but with a reduction in peak negative moment.

Pressure-coefficient contour plots of the case with and without controlled flap

actuation are shown in Figure 11. As the flap is deflected upwards, the pressure gradient between the upper and lower surfaces of trailing edge of the airfoil is reduced. This results in a slight displacement of the stall vortex and considerable change to the negative pitching moment coefficient.

VR-7 with Controlled Leading-Edge Slat

The effectiveness of dynamic stall mitigation using a leading-edge slat was also investigated. The slat geometry was obtained from a previous study published in Reference 7. For fair comparison, the slat is added to the VR-7 airfoil with the trailing-edge flap configuration. Two strategies for slat motion were considered.

The slat is scheduled to move sinusoidally in positive or negative direction of V_t and V_n as shown in Figure 12. Two cases were computed with slat maximum translation of 0.8 % chord with negative V_n (slat-norm1/flap) and positive V_n (slat-norm2/flap). A case with stationary slat (slat-flap) was also computed for the sake of comparison. Two cases with the slat moving sinusoidally in negative V_t (slat-tan1/flap) and positive V_t (slat-tan2/flap) were computed with slat maximum translation of 1.3% chord. A case of slat move in negative V_t (slat-tan3/flap) with maximum translation of 2.6% chord was also investigated. Six simulations of VR-7 with leading-edge slat were computed with $\delta_f = 0^\circ$. Figure 13 shows the time history of dynamic lift, and pitching moment coefficients using SST turbulence model, and compared with the cases of the VR-7 airfoil with and without flap. The hysteresis of lift and moment plots show that airfoil with leading-edge slat has no evidence of a stall vortex even at such a high angle of attack oscillation. Moreover, the lift-slope curve has been improved by the addition of

the slat. The stationary slat configuration shows a spike in pitching moment around $\alpha = 25^\circ$ while the “slat-norm1/flap” and “slat-tan1/flap” cases maintain an average of zero pitching moment during the pitching cycle. The “slat-norm2/flap”, “slat-tan2/flap” and “slat-tan3/flap” cases show slightly negative pitching moment in the region of $\alpha = 25^\circ$. Comparing the tangential motion of the slat with translation amplitude of 1.3% (slat-tan1/flap) and 2.6% (slat-tan3/flap) chord, the latter shows a slight gain in lift at high angle of attack but a loss in lift for the down-stroke cycle. This may be attributed to the increase and decrease in camber during the up-stroke and down-stroke of the cycle, respectively.

Results indicate the strategy of sinusoidal motion of slat in V_t and V_n can also eliminate the spike in pitching moment of the stationary slat case (slat/flap) at the end of the up-stroke cycle. Figure 14 presents snapshots of instantaneous streamlines colored by Mach number for six different cases at the maximum α of 25° . There is no dynamic stall vortex apparent in the flow-field; however, separation does occur over the aft portion of the main airfoil. Streamline plots indicate that the addition of a slat to the VR-7 airfoil relieves the adverse pressure gradient on the nose of the main airfoil, and the forward portion of the main airfoil appears attached. The different slat motions play an important role in controlling the separation region moving forward of the airfoil’s upper surface during the pitching oscillation.

Figure 15 presents the vorticity contour plots of the corresponding pitch angle. Vorticity generated by the slat is shed at a large enough distance above the main airfoil and energizes the flow downstream to delay the trailing-edge separation. Comparing the normal motion of slat of “slat-norm1” and

“slat-norm2”, slat (slat-norm2), which moves in a positive V_n direction, is more effective in controlling trailing-edge flow separation. Slat (slat-norm1), which moves in a negative V_n direction, could lose its effectiveness because the influence of the vorticity ushering downstream is greatly reduced (slat-norm1 of Figure 15). All three cases of the slat moving in the V_t direction show greater effectiveness in controlling the upstream movement of trailing-edge separation.

Concluding Remarks

FUN3D unstructured mesh flow solver was used to investigate flow over an oscillating Boeing VR-7 airfoil section. The dynamic stall characteristics of the Boeing VR-7 airfoil were computed using Spalart-Allmaras, and Menter shear-stress-transport $k-\omega$ turbulence models. The force, pitching moment and surface-pressure coefficients were computed and compared with experimental data. Computed results using the two-equation turbulence model show better correlation with experiment. Two actively controllable devices in the form of trailing-edge flap and leading-edge slat were considered to modify the same airfoil to mitigate dynamic stall effects. The basic findings of this study were as follows:

1. The addition of a trailing-edge flap on a VR-7 airfoil without schedule actuation can reduce the magnitude of negative pitching moment. The clearance between the airfoil and flap has a relieving effect on the dynamic stall behavior.
2. The addition of a trailing-edge flap on a VR-7 airfoil with sinusoidal motion about the flap hinge opposite to the main airfoil can delay stall and reduce negative peak pitching moment.
3. The flap strategy permits the stall to occur at the main airfoil. The flap

deflection at the trailing edge upwards serves to reduce the pressure gradient between the upper and lower surface of trailing edge of the airfoil. This results in a slight displacement of the stall vortex and considerable change to the negative pitching moment coefficient.

4. The addition of a stationary or moving leading-edge slat on a VR-7 airfoil completely eliminates the development of a dynamic vortex during unsteady pitching motion. Vorticity generated by the slat is shed at a large enough distance above the main airfoil and energizes the flow downstream to delay the trailing-edge separation.
5. The strategies for the leading-edge slat motion during pitching oscillation play an important role in obtaining better dynamic stall characteristics.

Acknowledgment

The author would like to thank Drs. Eric Nielsen, Robert Biedron and Ms. Beth Lee-Rausch of the NASA Langley Research Center for providing technical support on FUN3D. The provision of leading-edge slat geometry by Dr. Chee Tung for this study is greatly appreciated. The computer resources of the Department of Defense Major Shared Resource Center and Distributed Center of the Space and Missile Defense Future Warfare Center are gratefully acknowledged.

References

- ¹ Martin, P. B., McAlister, K. W., Chandrasenkara, M. S., and Geissler, W., “Dynamic Stall Measurements and Computations for a VR-12 Airfoil with a Variable Droop Leading Edge,” 59th AHS Annual Forum, Phoenix, Arizona, May 2003.

- ² Geissler, W., Ditzz, G., and Mai, H., “Dynamic Stall and Its Passive Control Investigations on the OA209 Airfoil Section,” 31st European Rotorcraft Forum, Firenze, Italy Sept. 2005.
- ³ Wong, T.-C., O’Malley, III, J. A., and O’Brien, Jr., “Investigation of Effect of Dynamic Stall and Its Alleviation on Helicopter Performance and Loads,” 62nd Annual Forum, Phoenix, Arizona, May 2006.
- ⁴ Nielsen, E. J., and Anderson, A. K., “Aerodynamic Design Optimization on Unstructured Meshes Using the Navier-Stokes Equations,” AIAA Paper 97-4809, 1997.
- ⁵ Nielsen, E. J., Lu, J., Park, M. A., and Darmofal, D. L., “An Implicit Exact Dual Adjoint Solution Method for Turbulent Flows on Unstructured Grids,” *Computers and Fluids*, Vol. 33, No. 9, pp. 1131-1155, November 2004.
- ⁶ Kinzel, M. P., Maughmer, M. D., Lesieutre, G. L., and Duque, E. P. N., “Numerical Investigation of Miniature Trailing-Edge Effectors on Static and Oscillating Airfoils,” AIAA 2005-1039, January 2005.
- ⁷ Wong, T-C, “The Impact of Advanced Airfoils on Rotor Hover Performance,” AIAA-2008-7342, August 2008.
- ⁸ Rumsey, C. L., “Consistency, Verification, and Validation of Turbulence Models for Reynolds-Averaged Navier-Stokes Applications,” 3rd European Conference for Aerospace Sciences, Paper EUCASS2009-7, 2009.
- ⁹ Lynch, C. E., Smith, M. J., “Hybrid RANS-LES Turbulence Models on Unstructured Grids,” AIAA Paper 2008-3854, June 2008.
- ¹⁰ Anderson, W. K., and Bonhaus, D. L., “An Implicit Upwind Algorithm for Computing Turbulent Flows on Unstructured Grids,” *Computers and Fluids*, Vol. 23, No. 1. pp. 1-21, 1994.
- ¹¹ Biedron, R. T., Vatsa, V. N., and Atkins, H. L., “Simulation of Unsteady Flows Using an Unstructured Navier-Stokes Solver on Moving and Stationary Grids,” AIAA Paper 2005-5093, June 2005.
- ¹² Roe, P. L., “Approximate Riemann Solvers, Parameter Vectors, and Difference Schemes,” *Journal of Computational Physics*, Vol. 43, No. 2, pp. 357-372, 1981.
- ¹³ Vatsa, V. N. and Carpenter, M. H., “Higher Order Temporal Schemes with Error Controllers for Unsteady Navier-Stokes Equations,” AIAA Paper 2005-5245, 2005.
- ¹⁴ Marcum, D. L., “Generation of Unstructured Grids for Viscous Flow Applications,” AIAA Paper 95-0212, 1995.
- ¹⁵ McAlister, K. and Tung, C., “Suppression of Dynamic Stall with a Leading-Edge Slat on a VR-7 Airfoil,” ATCOM Technical Report 92-A-013 or NASA TP 3357, March 1993.
- ¹⁶ McAlister, K. W., Pucci, S. L., McCrosky, W. J., and Carr, L. W., “An Experimental Study of Dynamic Stall on Advanced Airfoil Sections Volume. Pressure and Force Data,” USAAVRADCOR TR-82-A-8 (or NASA TM 84245), Sept. 1982.

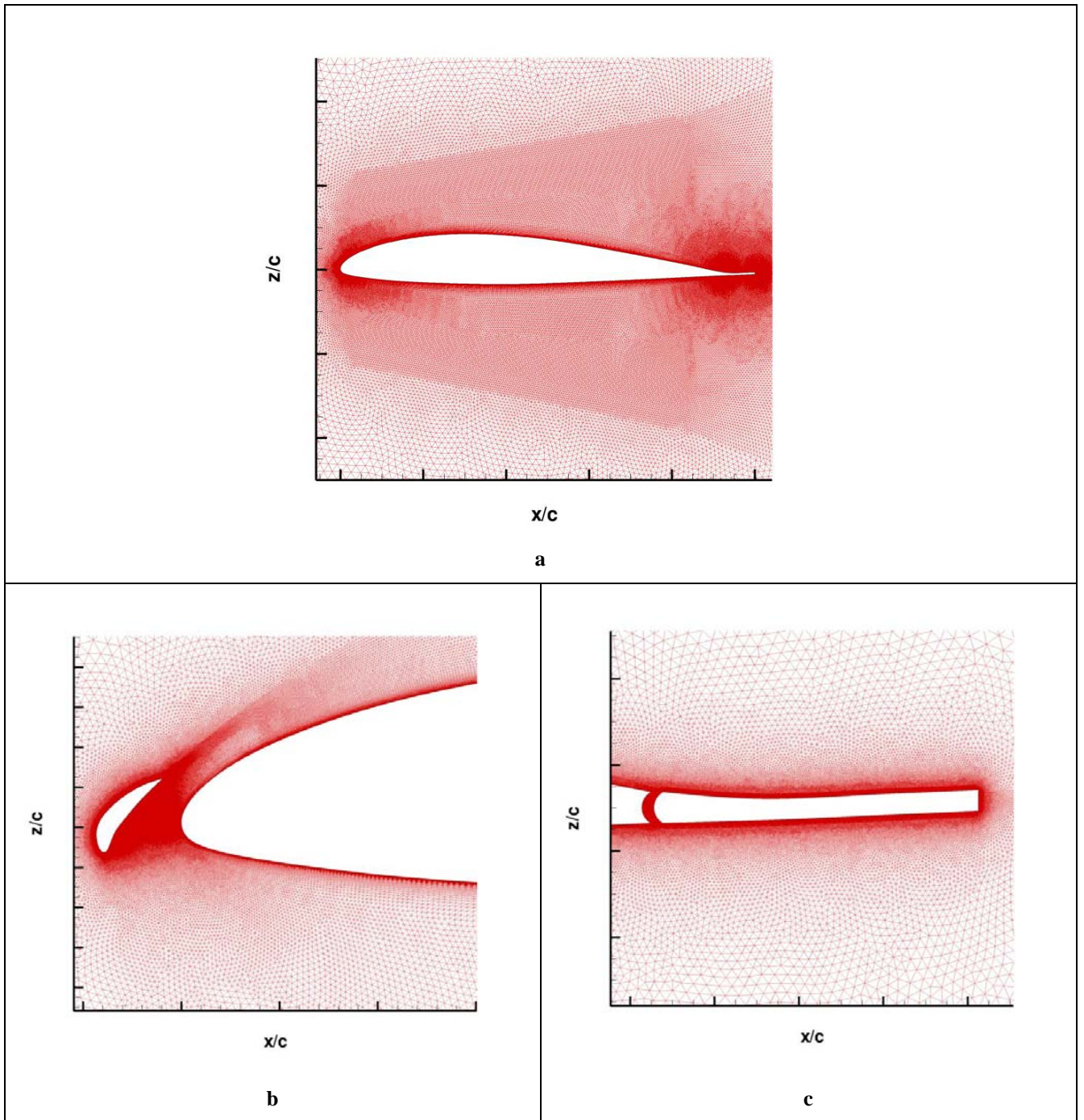


Figure 1 Three Unstructured Meshes of VR-7 Airfoils - (a) Baseline, (b) Close-up of VR-7 Airfoil with Leading-Edge Slat and (c) Trailing-Edge Flap.

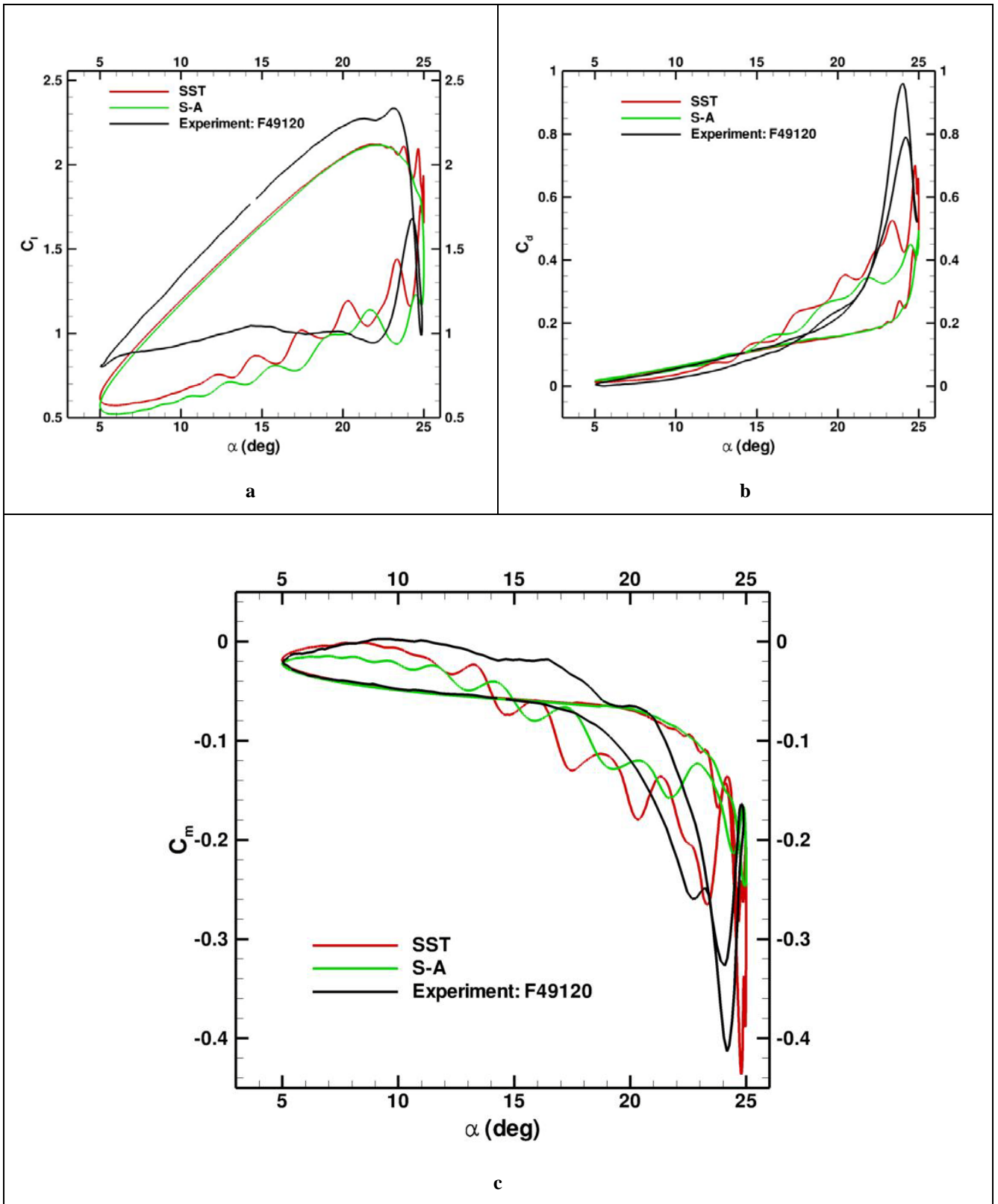


Figure 2 Comparison of Lift (a), Drag (b) and Pitching Moment (c) of Baseline VR-7 Airfoil with Wind Tunnel Test Data.

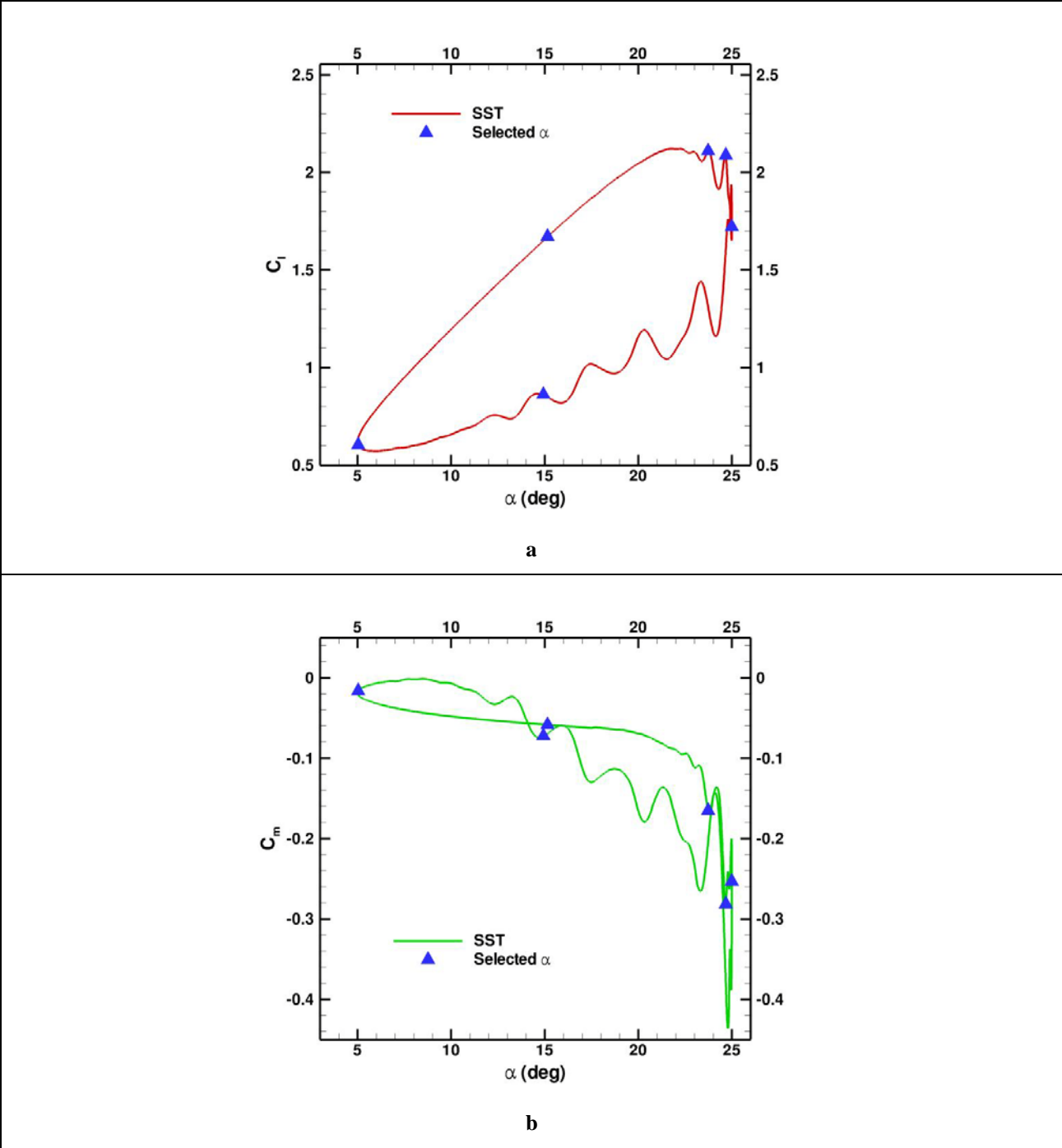


Figure 3 The Corresponding Values of α along the (a) Lift and (b) Pitching Moment Curves Chosen for Data Comparison.

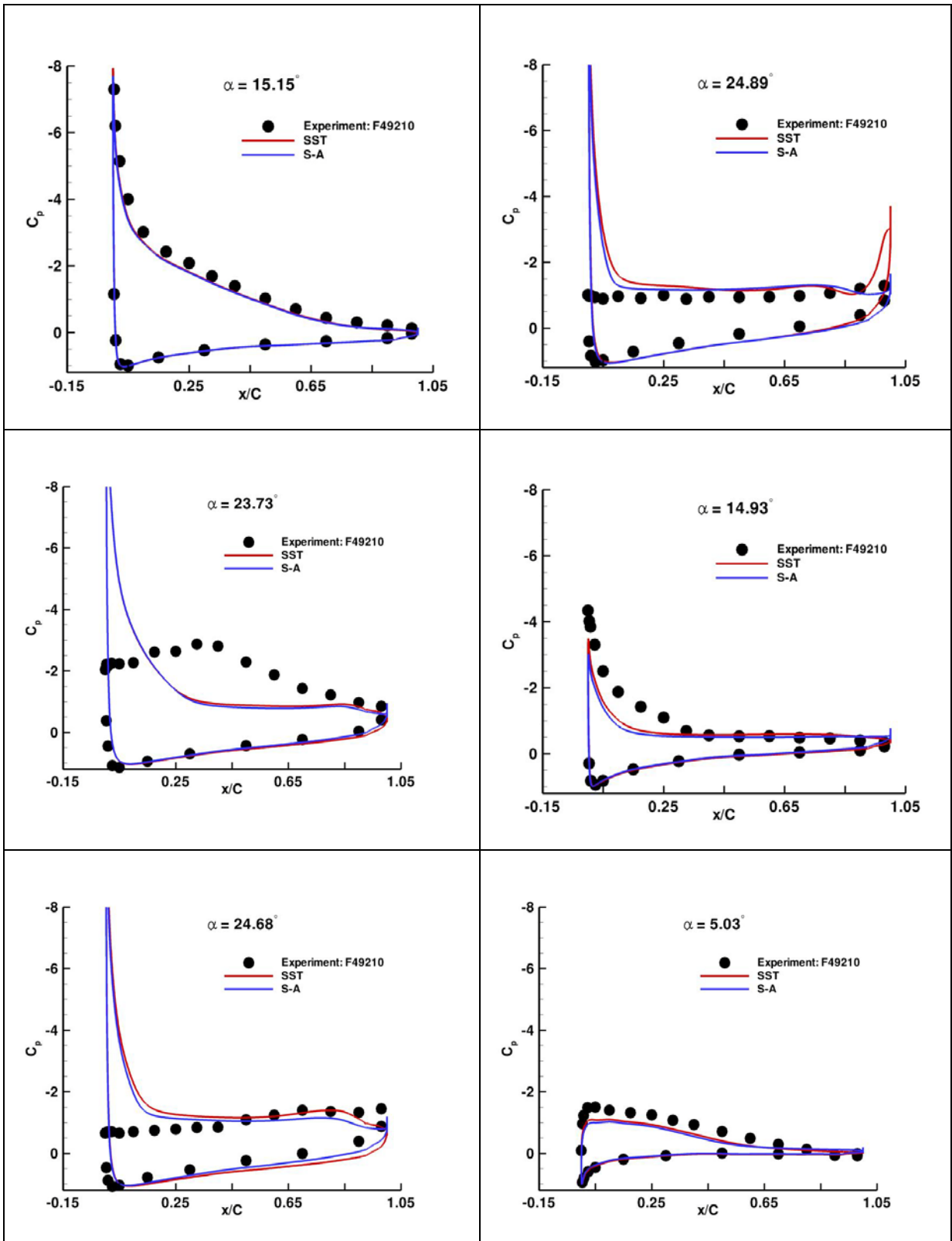


Figure 4 Comparison of Computed Surface-pressure Coefficients from SST and S-A with Experimental Data (Left: Pitch Up; Right: Pitch Down).

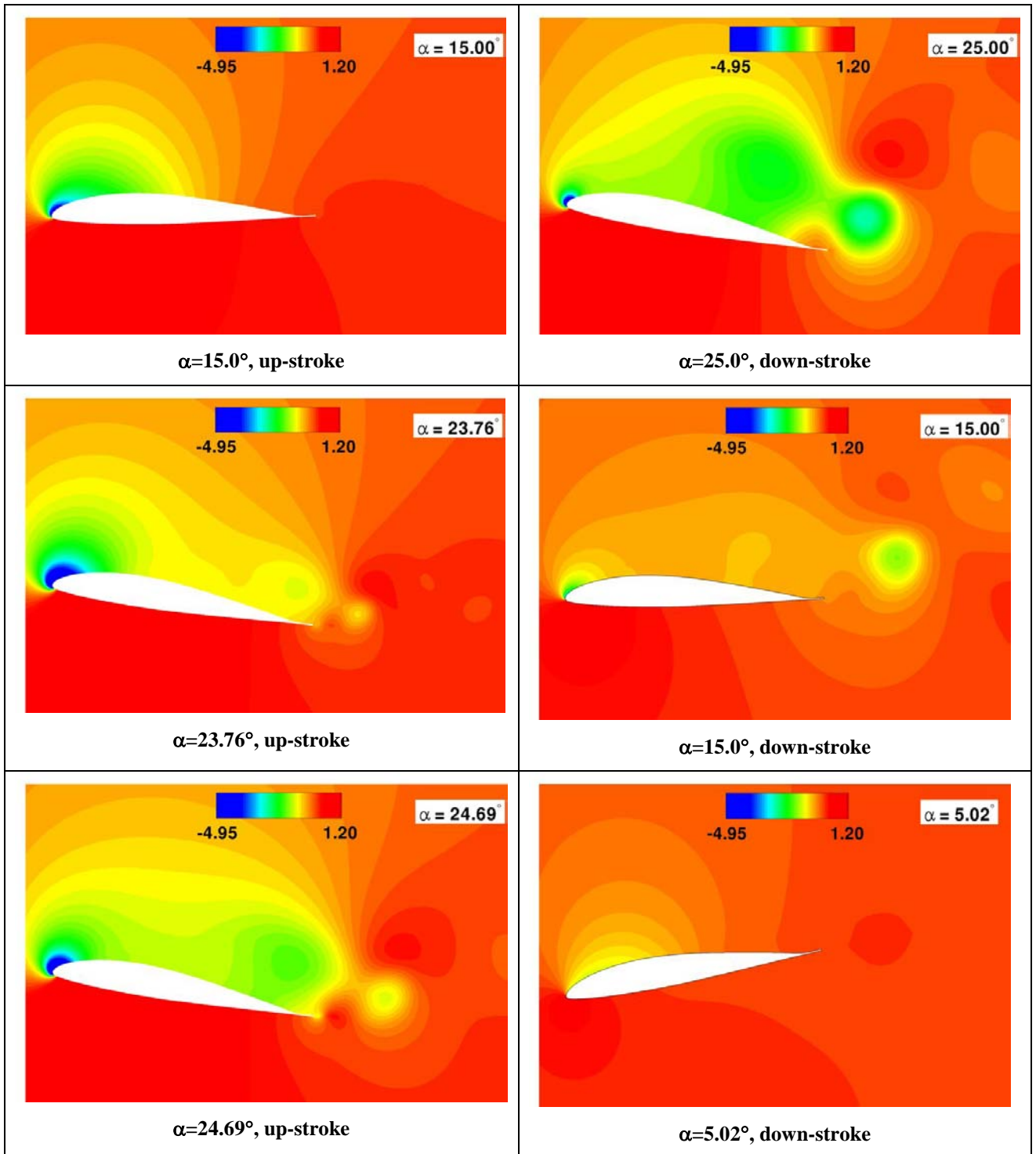


Figure 5 Pressure Coefficient Contour Plots of VR-7 Baseline Airfoil with SST Model at the Selected Pitch Angles.

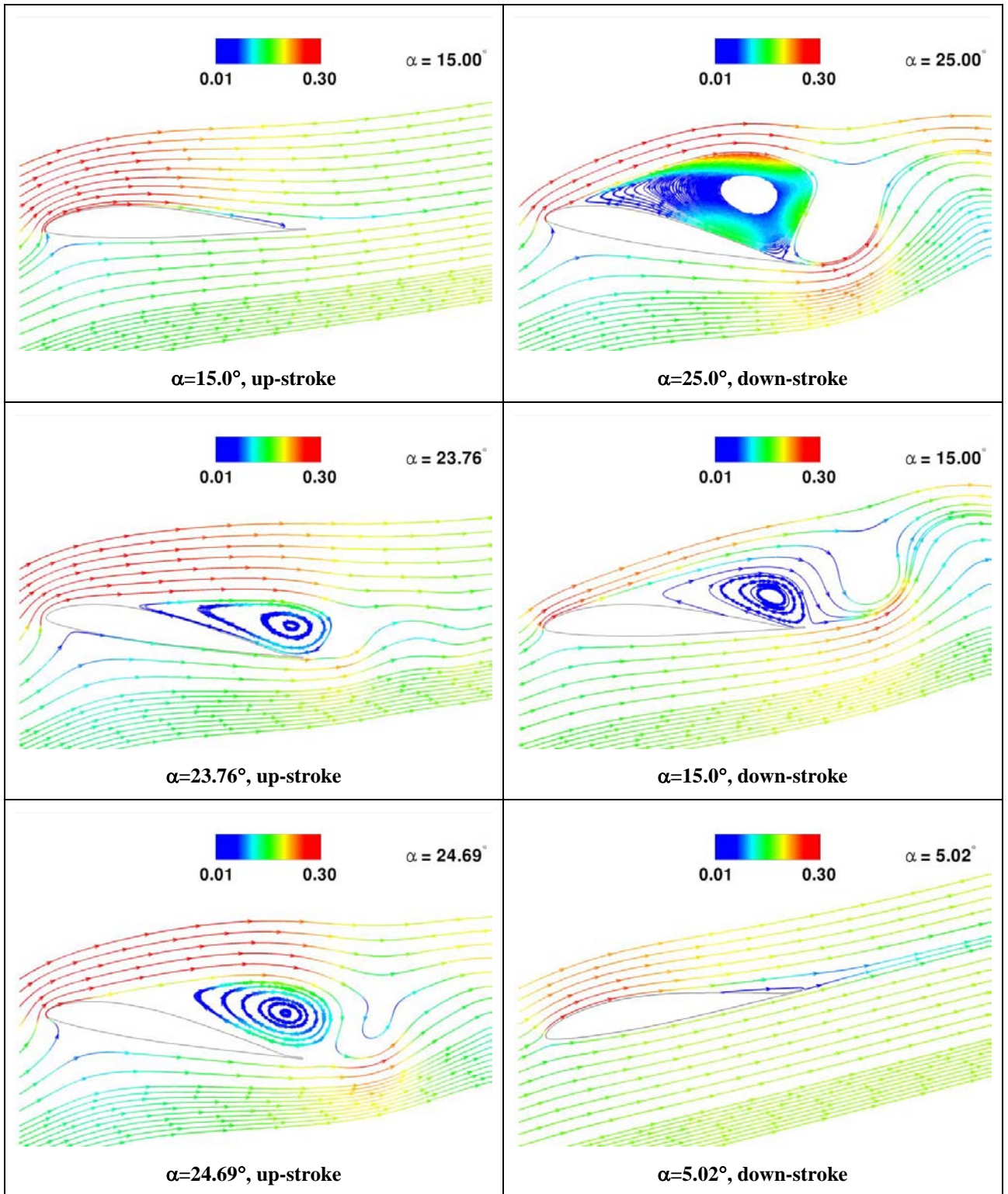


Figure 6 Instantaneous Streamlines Plots of VR-7 Baseline Airfoil with SST Model at the Selected Pitch Angles.

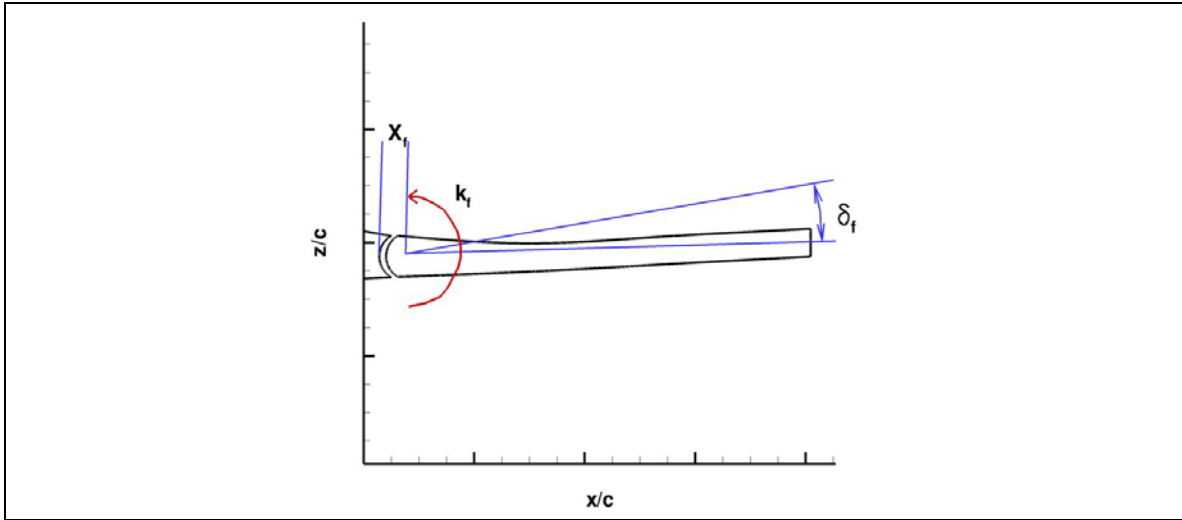


Figure 7 Layout of Modified Baseline VR-7 Airfoil with Trailing-edge Flap.

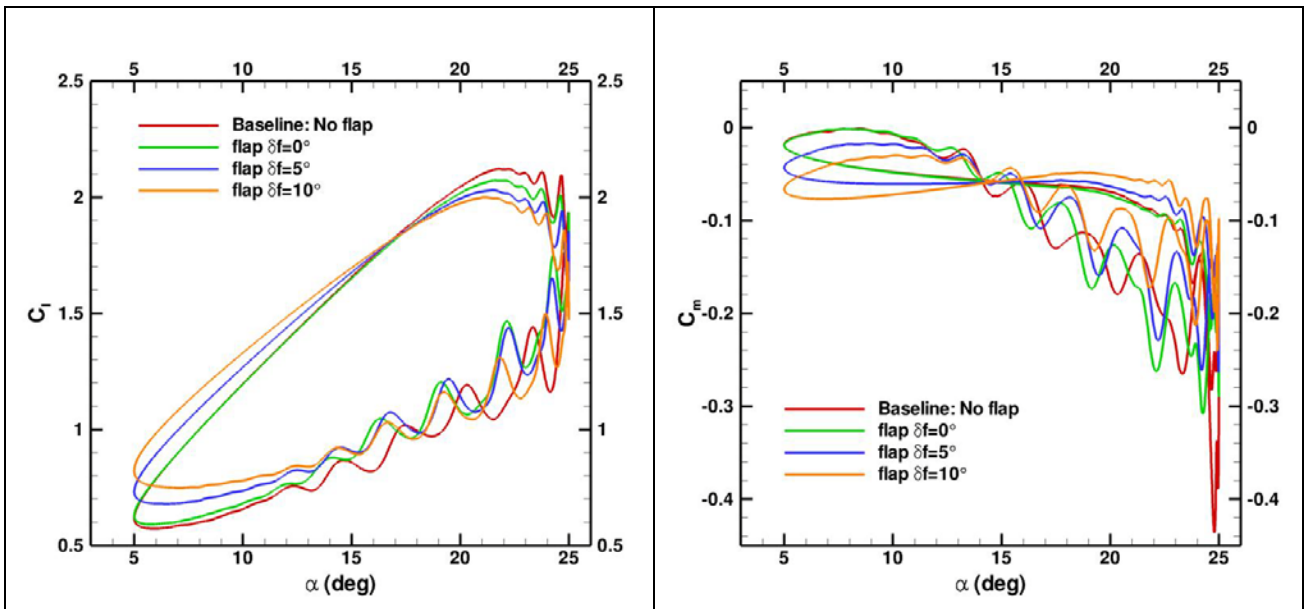


Figure 8 Comparison of Lift and Pitch Moment Coefficients of VR-7 with Trailing-edge Flap at Different Actuations.

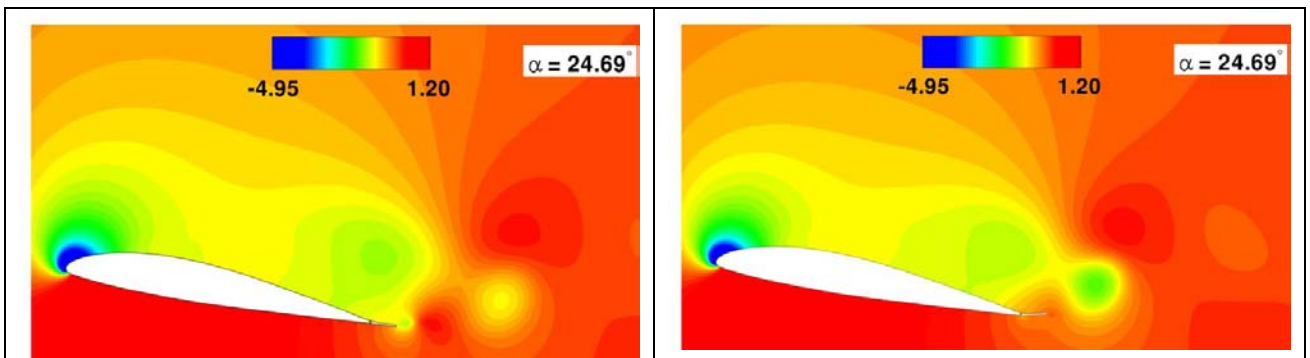


Figure 9 Pressure-Coefficient Contour of VR-7 with Trailing-edge Flap of $\delta_f = 0^\circ$ (left) and $\delta_f = 10^\circ$ (right).

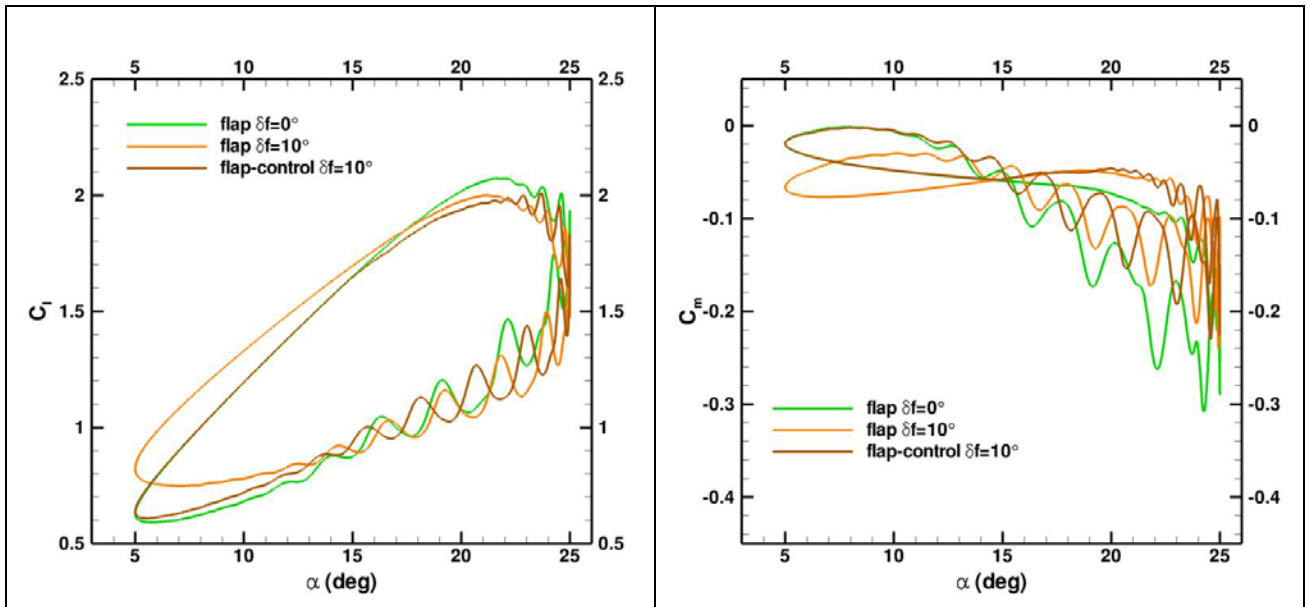


Figure 10 Comparison of Lift and Pitch Moment Coefficients of VR-7 with Trailing-edge Flap at Different Actuations.

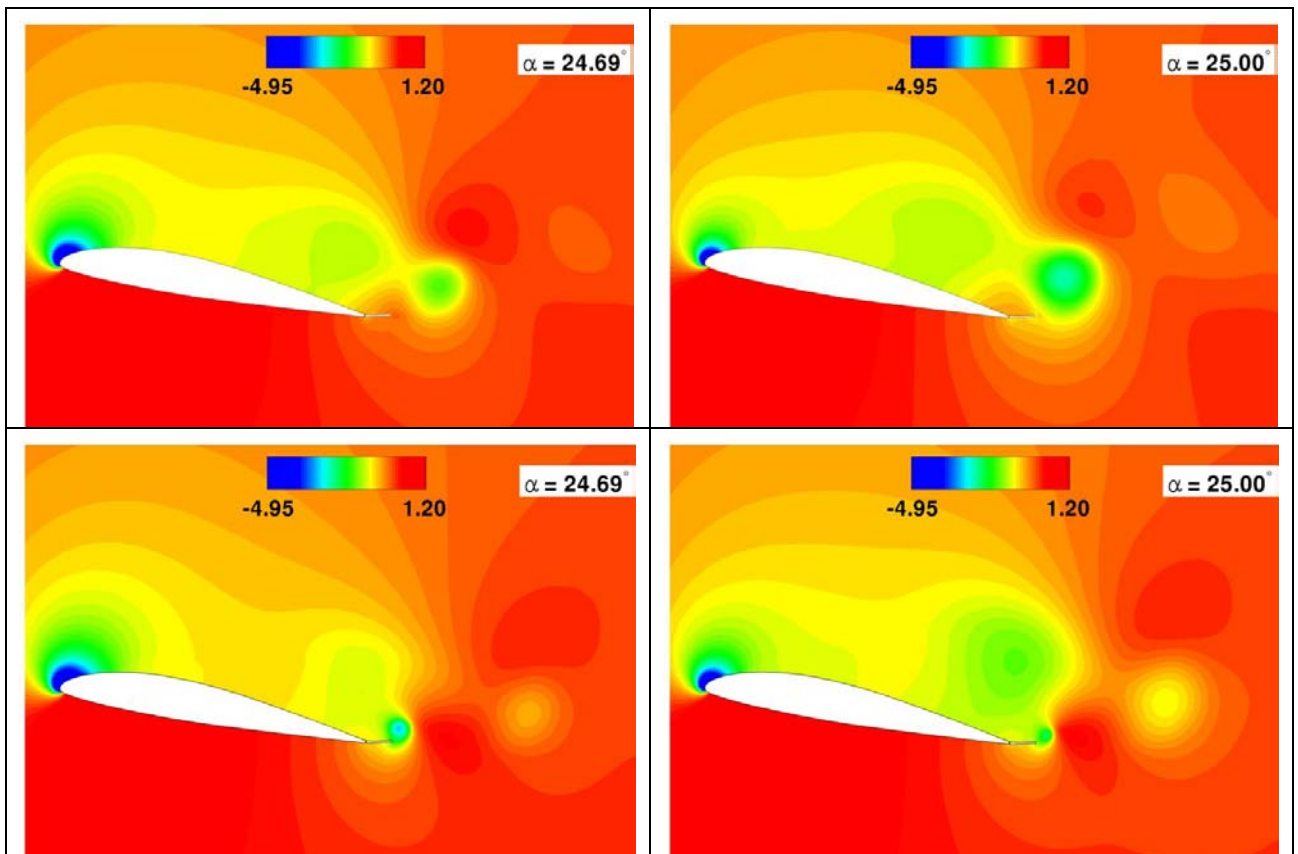


Figure 11 Pressure Coefficient Contour of VR-7 with Trailing-edge Flap of uncontrolled (top) and controllable $\delta_f = 10^\circ$ (bottom).

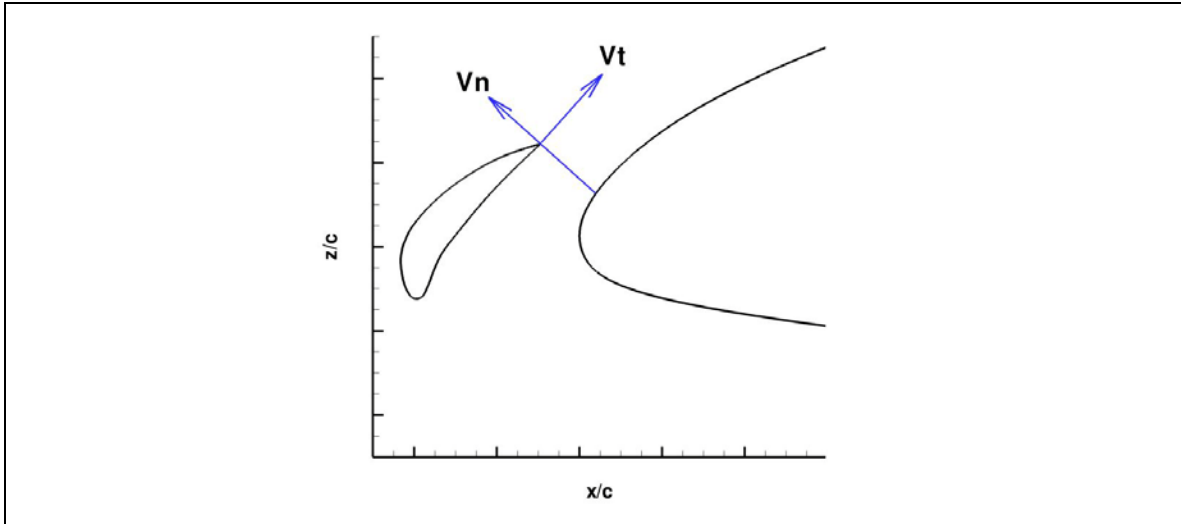


Figure 12 Layout of Modified VR-7 Airfoil with Leading-edge Slat.

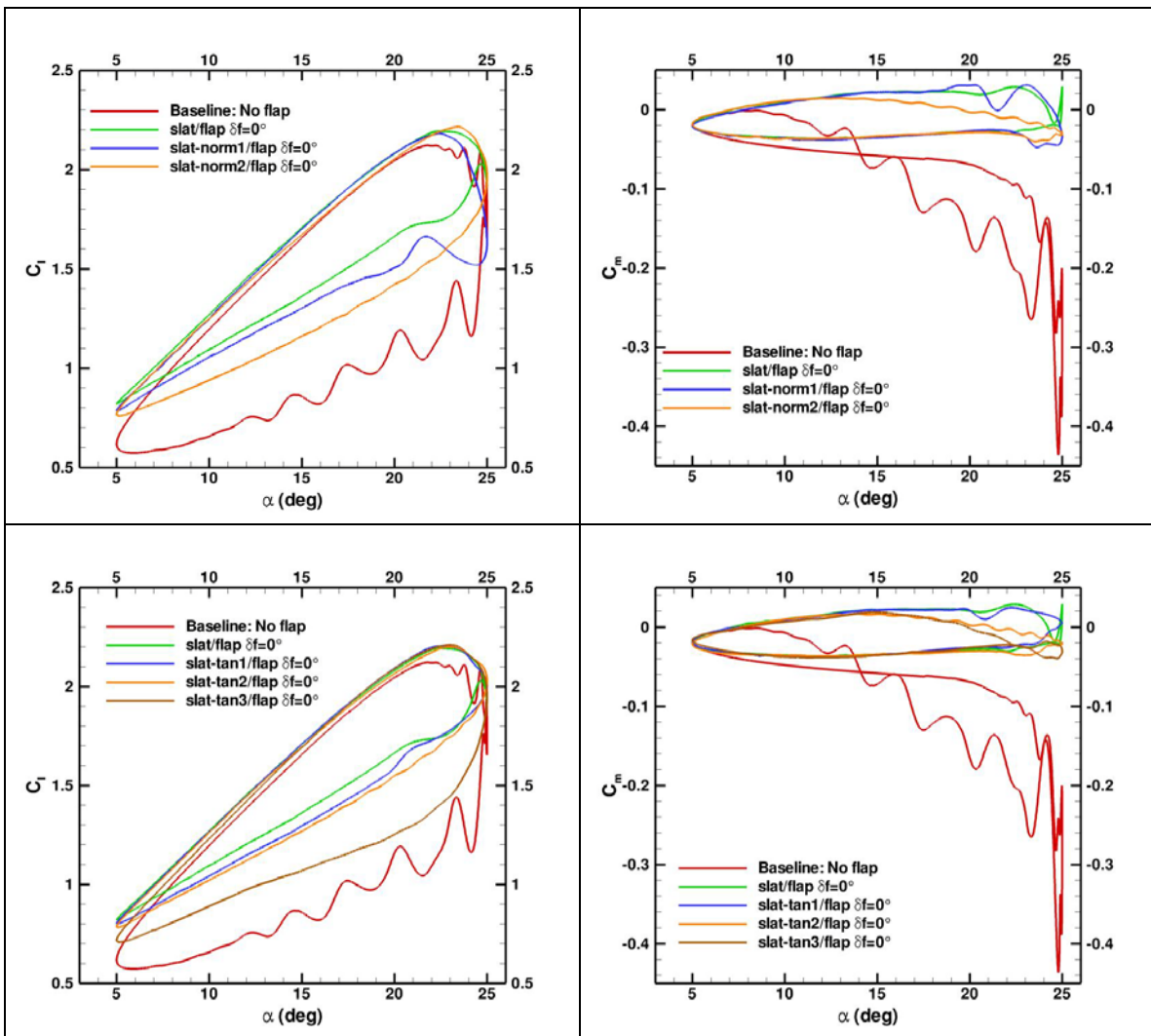


Figure 13 Comparison of Lift and Pitching Moment Coefficients of VR-7 Airfoil with Leading-edge Slat at Different Slat Motions.

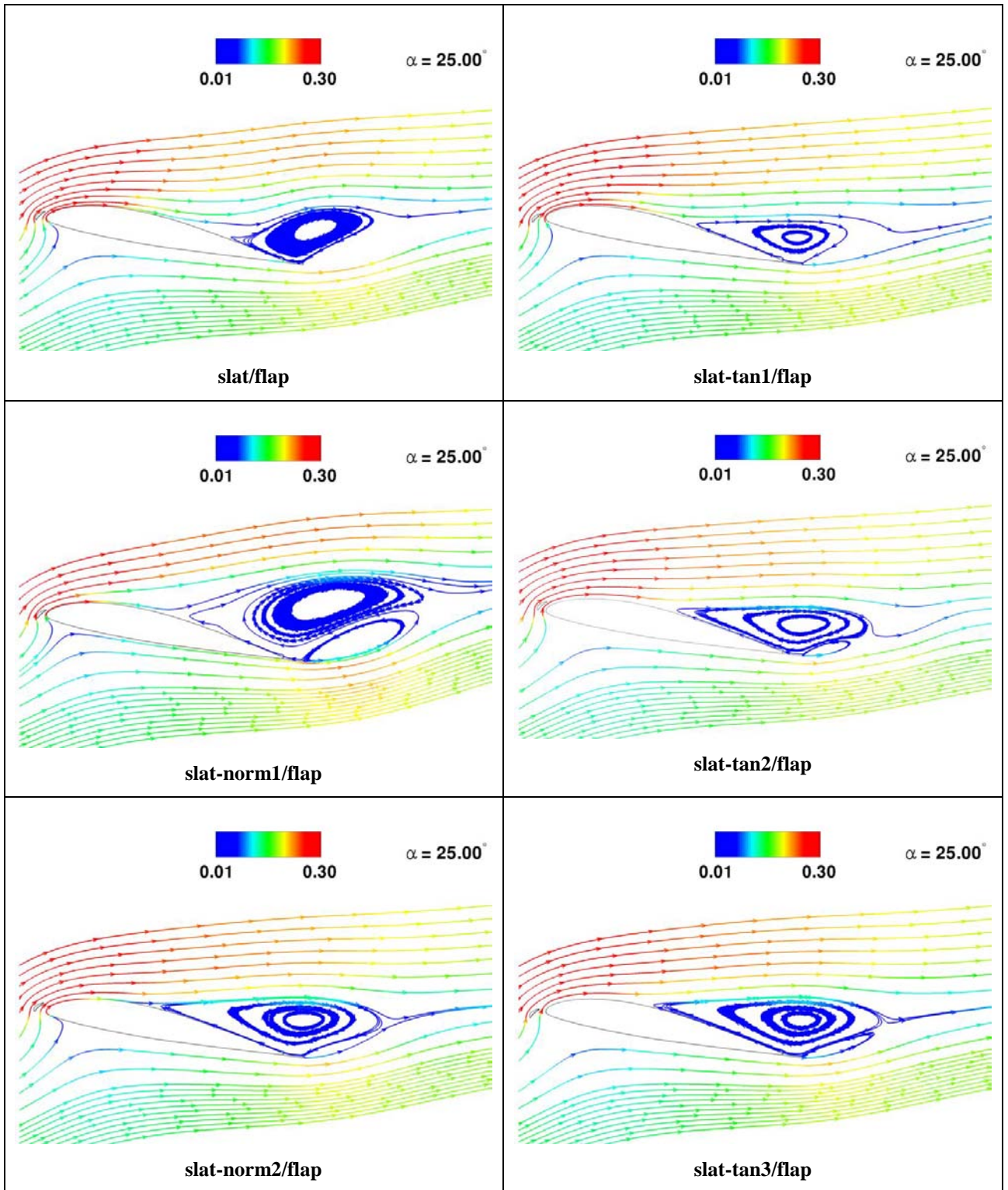


Figure 14 Instantaneous Streamline Plots of VR-7 Airfoil with Leading-edge Slat at Different Slat Motions.

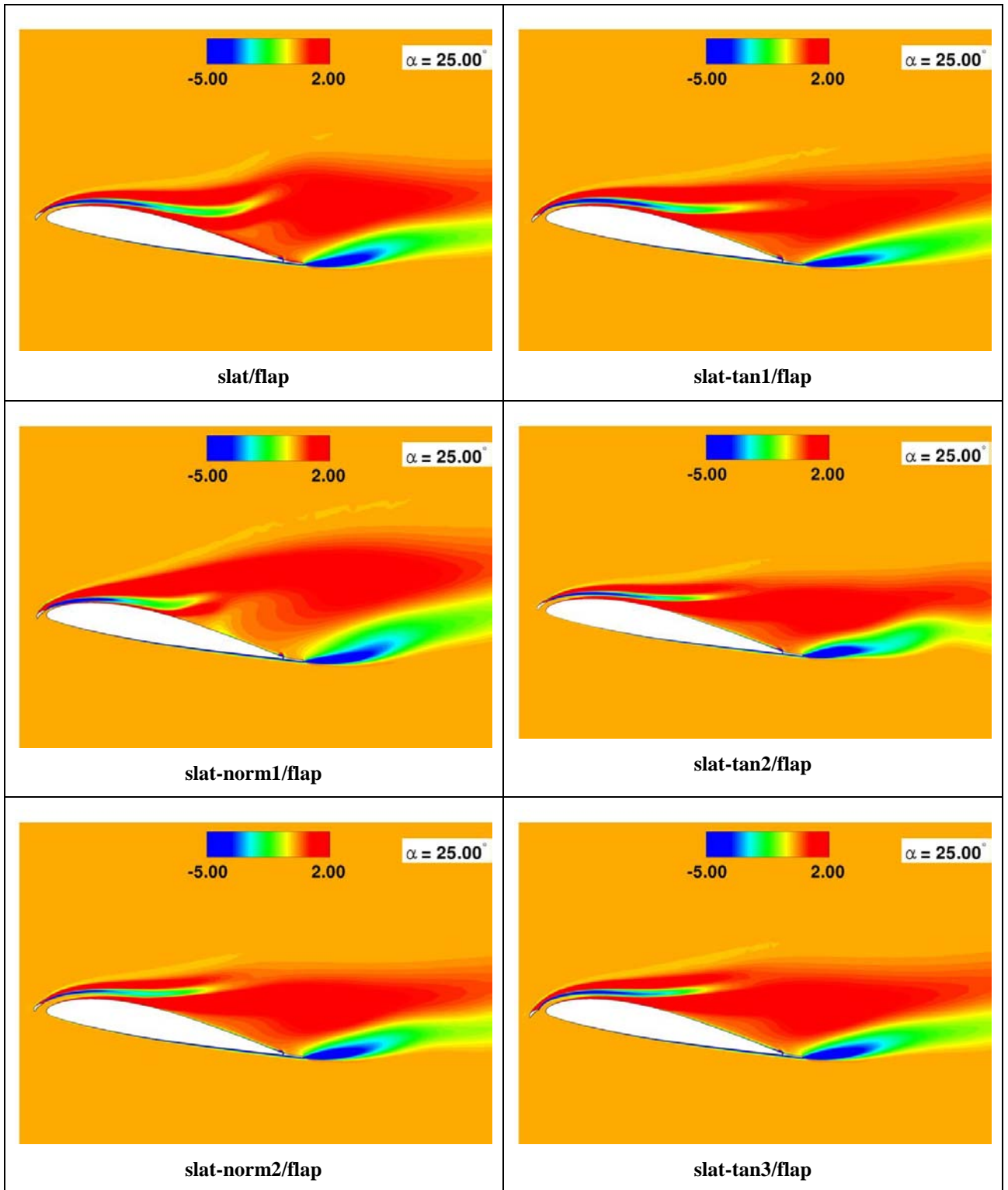


Figure 15 Vorticity Contour Plots of VR-7 Airfoil with Leading-edge Slat at Different Slat Motions.